ACS Photonics

pubs.acs.org/journal/apchd5

Article

Visible Elimination, Ultraviolet and Near-Infrared Dual-Band Photodetector Based on Single-Crystal Perovskite Heterojunctions Toward Secure Optical Communication

Yuzhu Pan, Xin Wang,* Dan Zhang, Ziyu Wei, Yubing Xu, Yuwei Li, Qing Li, Zhiwei Zhao, Zhuoya Zhu, Byung Seong Bae, Damian Chinedu Onwudiwe, Xiaobao Xu, and Wei Lei*

Cite This: *ACS Photonics* 2024, 11, 1252−1263

Read Online

ACCESS | Metrics & More | Article Recommendations | Supporting Information

ABSTRACT: Conventional photodetectors (PDs) sense either a broad waveband light or a selective narrow waveband light, which is plagued by indistinguishable diverse wavebands and is not competent for the dual task of information transfer and encryption in optical communication with an open light transmitting channel. Dual-band PDs with the ability to sense two discrete waveband lights have the potential to remedy the drawbacks of single-band PDs and realize secure optical communication with a straightforward optical encryption strategy. However, previous reports of dual-band PDs usually relied on multistacked photosensitive layers, which suffer from lattice mismatched interfaces contacting between diverse semiconductor layers and complex device fabrication processes. Herein, we propose a novel lattice-matched single-crystal perovskite heterojunction (SCPH) through a facile and low-cost liquid-phase epitaxy process. The fabricated dual-band PD with a structure of Au/$MAPbCl_3$/Bi-$MAPbBr_3$/Bi-$MAPbI_{2.5}Br_{0.5}$/$MAPbI_3$/Au senses to a broad range of ultraviolet (UV) light and a narrow range of near-infrared (NIR) light while blinding to visible lights in between. At last, a chaos-based double-encrypted secure optical communication system is built using the fabricated UV/NIR dual band SCPH PD as an efficient receiver terminal, where valid information is conveyed by UV and NIR light, respectively, and further superimposed by visible light for separately encrypted transmission. This work provides a facile method to fabricate visible-eliminating UV/NIR dual-band PDs and offers new insights into security optical communication without relying on complicated algorithms.

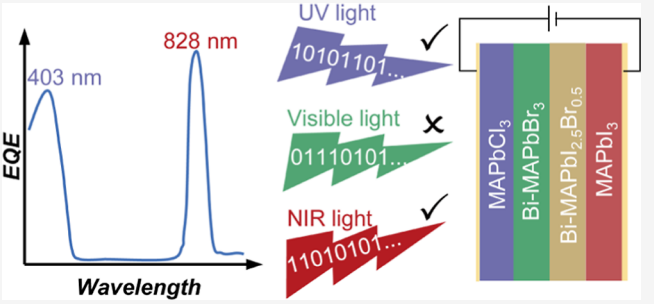

KEYWORDS: *dual-band detection, band elimination, perovskite heterojunction, optical communication, encryption technology*

INTRODUCTION

As a class of equipment with the ability to convert optical signals into electrical signals, photodetectors (PDs) are crucial components in modern optical-electrical interconnect systems, such as optical communication, digital imaging, remote sensing, medical and biological analysis, etc. The present commercially available PDs based on mature semiconductors as sensitive layers, such as silicon and some compounds (InGaAs, HgCdTe, ZnO...), belong to broadband photodetectors (BPDs), which are sensitive to a wide range of wavebands corresponding to their absorption spectra.[1−4] Some PDs have the ability to selectively detect a specific range of wavebands and belong to narrowband photodetectors (NPDs) by adopting various strategies, including adding dedicated bandpass filters,[5] using narrowband absorbing photoactive materials,[6] microcavity structure design,[7,8] charge collection narrowing concept,[9,10] charge injection narrowing concept,[11,12] and heterostructure PD design.[13−15] However, traditional BPDs and NPDs still hardly satisfy the needs of application scenarios. Because BPDs may face severe signal interference due to their response to a wide range of wavelengths of light outside of the desired detection band, using NPD responding only to a single waveband may face the risk of signal leakage if the wavelength of the propagating signal is leaked.[16] Compared to the above single broadband or narrowband PDs, dual-band PDs are more attractive due to the capability of obtaining two discrete waveband photon information simultaneously, which could upgrade the capacity of photodetection in a complex environment and expand the applications in various scenarios.[17] Especially in chaos-based optical communication, to enhance data security during light wave transmission in open channels, only using a specific dual-band PD as the receiver terminal can decode valid information in a dual-channel optical

Received: December 5, 2023
Revised: February 11, 2024
Accepted: February 12, 2024
Published: February 26, 2024

https://doi.org/10.1021/acsphotonics.3c01768
ACS Photonics 2024, 11, 1252−1263

signal encrypted and modulated in different forms.[16,18−21] It increases the difficulty of signal decoding if the correct modulation wavelengths are not known.

Integrating spectral selectivity into a single pixel without using an external sophisticated filter or optical components is the current trend in making advanced miniaturization dual-band PDs.[22,23] To realize specific dual-band spectral detection, a series of ultraviolet (UV)/UV, UV/visible, UV/infrared (IR), visible/IR, and IR/IR dual-band PDs have been proposed.[17,24−27] However, these dual-band PDs are generally fabricated by two or more different photosensitive materials with alloy, superlattice, and multiple quantum well structures, requiring sophisticated instruments during the construction process such as molecular beam epitaxy, metal organic chemical vapor deposition, atomic layer deposition, and so on,[24,25,28] which inevitably suffer from shortcomings such as lattice and thermal mismatch between the semiconductor layers, high fabrication complexity, low production yield, and high costs.[22,29] Therefore, it is desirable to explore novel PDs with dual-band sensing capability through a simpler device structure and a more cost-effective fabricating process.

In recent years, due to their relatively low processing costs and prominent properties, including a large light absorption coefficient, a long carrier recombination lifetime, long and balanced exciton diffusion lengths, and high carrier mobility, perovskites have been considered promising light-harvesting materials to promote the progress of optical-electrical detection.[30,31] Especially for the metal hybrid halide perovskites (ABX_3, where A = MA^+, FA^+, Cs^+, B = Pb^{2+}, Sn^{2+} and X = Cl^-, Br^-, and I^-), they present great potential in spectroscopic detection with a range from UV to IR due to their tunable directed bandgap through adjusting halide composition.[32] These achievements of perovskite-based PDs reported by research, however, are mainly focused on the improvement of detection performance in either a broad range or a specific narrow waveband. Though a few progresses have been made in perovskite to obtain a dual-band response signal, including presenting distinct spectral responses under bidirectional light illuminations,[18,33] building electrically modulated back-to-back rectifying junction diode configuration,[20,22,34] adopting tandem vertically stacked device structure,[35] fabricating bulk heterojunction,[16] using two-photon absorption effect,[36] etc. Overall, investigations of dual-band PDs based on perovskite materials are still in their infancy. One of the important issues to realize dual-band detection using perovskite as a photosensitive layer is how to eliminate photoelectric response out of the target detection waveband. The incorporation of bismuth ions into perovskites will change their optical and electrical properties due to the introduction of defects,[37−39] which has been proven to be an efficient way to adjust the photoelectric response of perovskite based PDs.[15,40]

Herein, we developed a novel perovskite single crystal heterojunction (SCPH), which tandem vertically combined four different bandgap single-crystalline perovskite layers (pristine $MAPbCl_3$, Bi^{3+} doped $MAPbBr_3$, Bi^{3+} doped $MAPbI_{2.5}Br_{0.5}$, and pristine $MAPbI_3$) without serious lattice mismatch between different perovskite layers, through a facile and low-cost liquid-phase epitaxial (LPE) method proposed in our previous works.[15,41−43] Attributed to the well-designed energy band engineering and discontinuous electric field distribution in the SCPH, we successfully obtained broad UV and narrow NIR dual-band spectral response detectors with visible waveband response elimination. The as-fabricated dual-band PD based on the SCPH can obtain a broadband response to the UV region with a cutoff wavelength of 403 nm with a responsivity of around 15 mA W^{-1}, and a narrowband response to the NIR region from 750 to 880 nm with a peak responsivity of 18 mA W^{-1} at 828 nm under an external voltage bias. Furthermore, the as-fabricated UV/NIR dual-band SCPH PD shows competitive detection performance, such as measured specific detectivity (D^*) greater than 10^{10} Jones and a response speed of hundreds of microseconds. According to the chaos-based security optical communication principle,[44] we successfully established a double-encrypted optical communication system by hiding the UV light signals and NIR light signals in random visible light signals for transmitting separately and using the specific dual-band SCPH-based PD as the receiver terminal. Only using a specific visible elimination, UV/NIR dual band PD, as a receiver to obtain twice-correct signals from double encrypted light transmissions can the final valid information be further decoded. The well-designed SCPH-based dual-band PD with such broadband UV and narrowband NIR detection abilities without visible light interference is expected to provide new opportunities and platforms for optical communication encryption techniques and bring this secure and reliable communication technology into real-life applications.

EXPERIMENTAL SECTION

Preparation of Chemicals and Reagents. *N*,*N*-Dimethylformamide (DMF), dimethyl sulfoxide (DMSO), and γ-butyrolactone (GBL) were obtained from Aladdin. Methylamine hydrochloride (CH_3NH_3Cl, 98%), methylammonium bromide (CH_3NH_3Br, 99.5%), and methylammonium iodide (CH_3NH_3I, 99.5%) were purchased from Macklin reagents. Lead chloride ($PbCl_2$, 99.99%), lead bromide ($PbBr_2$, 99.99%), lead iodide (PbI_2, 99.99%), bismuth(III) chloride ($BiCl_3$, ≥98%), bismuth(III) bromide ($BiBr_3$, ≥98%), and bismuth-(III) iodide (BiI_3, ≥98%) were purchased from Sigma-Aldrich. All commercial products were used as received without any further purification.

Fabrication of the SCPH. To prepare the precursor solution of $MAPbCl_3$, the equimolar ratio of CH_3NH_3Cl and $PbCl_2$ was dissolved in a mixed solvent of DMF and DMSO (the volume ratio was 1:1) at room temperature with a concentration of 1 mol L^{-1}. To prepare the precursor solution, 10% Bi^{3+} ions doped with $MAPbBr_3$, CH_3NH_3Br, $PbBr_2$, and $BiBr_3$ in a 1:1:0.1 molar ratio were dissolved in DMF at room temperature with a concentration of 1 mol L^{-1}. To prepare the precursor solution of 10% Bi^{3+} ions doped $MAPbI_{2.5}Br_{0.5}$, CH_3NH_3I, $PbBr_2$, PbI_2, and BiI_3 in a 1:0.25:0.75:0.1 molar ratio were dissolved in a mixed solvent of DMF and GBL (the volume ratio was 1:1) at a temperature of 70 °C with a concentration of 1.2 mol L^{-1}. To prepare the precursor solution of $MAPbI_3$, CH_3NH_3I, and PbI_2 in a 1:1 molar ratio, they were dissolved in GBL solvent at a temperature of 60 °C with a concentration of 1.5 mol L^{-1}. All fully dissolved perovskite precursor solutions were filtered through a PTFE filter with a 2.2 μm pore size for further process.

$MAPbCl_3$ ($MA^+ = CH_3NH_3^+$) single crystals with a size of several millimeters were grown by heating the 20 mL $MAPbCl_3$ precursor solution in a flat-bottom crystallizing dish from 30 to 60 °C in dozens of hours. The grown $MAPbCl_3$ bulk crystals were finally ground and polished into thin wafers hundreds of micrometers thick using different mesh sandpapers in sequence (mesh 800, mesh 4000, mesh 10,000,

https://doi.org/10.1021/acsphotonics.3c01768
ACS Photonics 2024, 11, 1252−1263

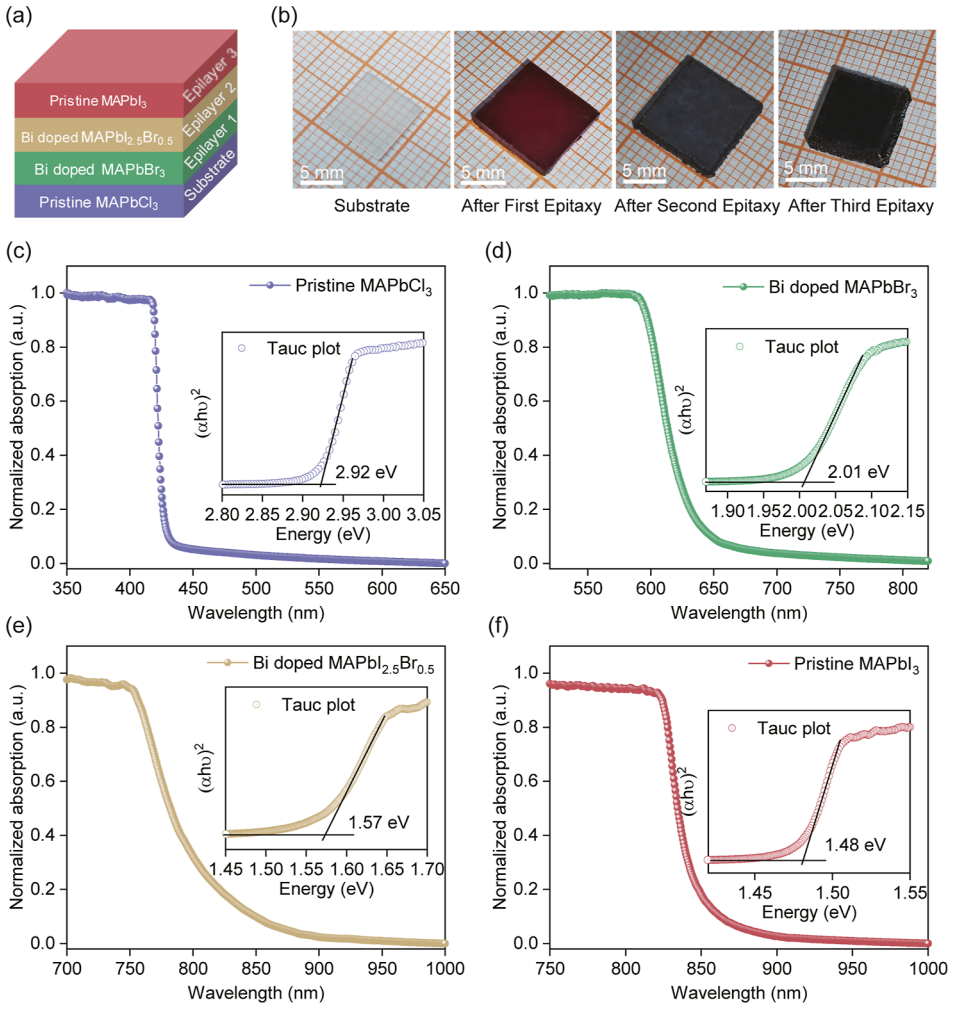

Figure 1. (a) Schematic cross-sectional configuration of the well-designed SCPH for UV/NIR dual-band detection. (b) Photographs of the heterojunction bulk after each LPE processing. (c–f) Normalized Vis-NIR absorption spectra of the $MAPbCl_3$, Bi-$MAPbBr_3$, Bi-$MAPbI_{2.5}Br_{0.5}$, and $MAPbI_3$ layers, respectively. Inset: corresponding Tauc plots were used to extract the bandgap.

mesh 15,000). The thin $MAPbCl_3$ wafers were immersed in a concentrated $MAPbCl_3$ precursor solution for 60 s after polishing to alleviate the mechanical damage on the surface. Finally, the residue on the surface of the polished thin perovskite wafers was rinsed in toluene to remove any possible surface contamination, and lens papers were usedto wipe dry.

The thin $MAPbCl_3$ perovskite single crystal wafers were dipped into the prepared 10 mL Bi-doped $MAPbBr_3$ perovskite precursor solutions to epitaxially grow for 2 h at 80 °C. After the first epitaxy, the heterojunction wafers were dipped into the prepared 10 mL Bi-doped $MAPbI_{2.5}Br_{0.5}$ perovskite precursor solutions to epitaxially grow for 1 h at 110 °C. After the second epitaxy, the heterojunction wafers were dipped into the prepared 10 mL $MAPbI_3$ perovskite precursor solutions to epitaxially grow for 0.5 h at 90 °C. The finally obtained $MAPbCl_3$/Bi-$MAPbBr_3$/Bi-$MAPbI_{2.5}Br_{0.5}$/$MAPbI_3$ SCPHs wafer is core–shell wrapped, and its surrounding redundant parts are cut away using a fine diamond-impregnated wire sawing machine. The thickness of epitaxial perovskite layers can be controlled by adjustments to the epitaxy duration in a precursor solution.

Characterization of Materials. X-ray photoelectron spectra (XPS) were obtained using a PHI 5000 VersaProbe (Japan). Optical absorption spectra were collected by LabTech's Bluestar-Series UV–vis spectrophotometers. X-ray diffraction (XRD) data were collected by a Switzerland X'TRA system with a Cu Kα target radiation source. The scanning electron microscopy (SEM) images were captured by a Quanta 200F environmental scanning electron microscope. Energy dispersive X-ray spectroscopy (EDX) analysis was carried out using an X-act Oxford Instrument system coupled with the SEM. Hall effect measurements were performed using a Hall measurement system (PM-50 MR Platform, EMT-2400 Data Acquisition System) with the van der Pauw protocol. The steady-state photoluminescence (PL) spectra were collected with an FS5 spectrofluorometer (Edinburgh Instruments, UK) at room temperature using a xenon lamp as the excitation source. The time-resolved PL (TRPL) measurements were performed using a picosecond pulsed diode laser as excitation and a time-correlated single-photon counting detector for signal collection.

Measurement of the PDs. Semitransparent gold films of about 30 nm were deposited on the two opposite surfaces of $MAPbCl_3$/Bi-$MAPbBr_3$/Bi-$MAPbI_{2.5}Br_{0.5}$/$MAPbI_3$ SCPH wafers as electrodes through thermal evaporation in vacuum to finally fabricate the SCPH-based devices. The measured I–V (current–voltage) and I–T (current–time) curves of the SCPH-based devices were obtained by a Keithley 2400

https://doi.org/10.1021/acsphotonics.3c01768
ACS Photonics 2024, 11, 1252–1263

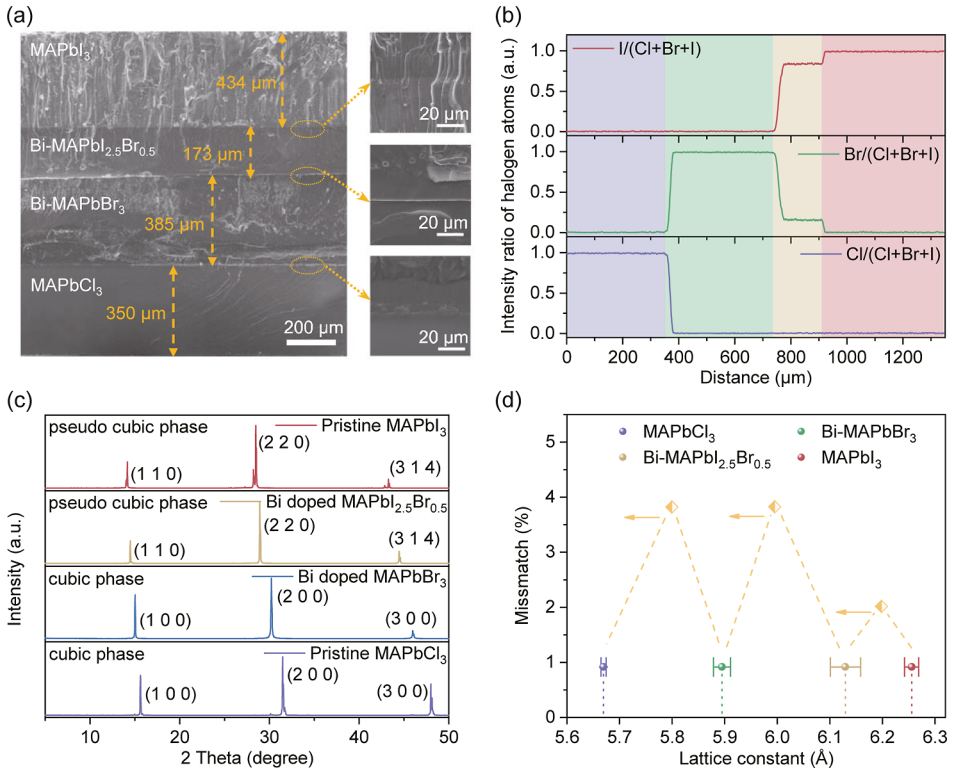

Figure 2. (a) Cross-sectional SEM image of epitaxially fabricated $MAPbCl_3$/Bi-$MAPbBr_3$/Bi-$MAPbI_{2.5}Br_{0.5}$/$MAPbI_3$ SCPH. (b) EDX line scanning results in plots of the halogen atom content intensity ratio across the whole cross-section of the SCPH. (c) XRD pattern of the independent $MAPbCl_3$, Bi-$MAPbBr_3$, Bi-$MAPbI_{2.5}Br_{0.5}$, and $MAPbI_3$ layers. (d) Mismatch rate between adjacent perovskite layers in the SCPH as a function of the lattice constant.

sourcemeter. The wavelength-dependent photocurrent was obtained by directly connecting SCPH based PDs to a Keithley 2400 sourcemeter and illuminating under different monochromatic light. The monochromatic light is prepared by an Xe lamp (CEL-HXF 300) attached with a monochromator (Zolix Instruments, Omni-λ200i) and is out from an optical fiber port. The power intensity of all light sources utilized in this paper was accurately calibrated by a power meter (Thorlabs GmbH., PM 100D). The noise current of the SCPH-based PDs was extracted from the Fourier transform of the dark current, which was monitored by an Agilent oscilloscope (7.5G, USA). For transient photocurrent measurement, the detector was biased using a Keithley 2400 sourcemeter, two monochromatic LEDs with a central wavelength of 365 and 805 nm were modulated by a function generator (square waves with a frequency of 10 Hz) as the excitation source, and a 100 kΩ resistance was connected in series with the detector to extract the signal by an Agilent oscilloscope (7.5 GHz, USA).

RESULTS AND DISCUSSIONS

The configuration of the well-designed SCPH for visible elimination and UV and NIR dual band detection is presented in Figure 1a. It is a compound single-crystalline bulk made by vertically epitaxially stacking four kinds of perovskite materials. Initially, transparent $MAPbCl_3$ single crystals were grown from precursor solution by inverse temperature crystallization and ground to hundreds of micrometers' thick wafers, which then acted as a substrate for further epitaxy processes. The single-crystalline layers of Bi^{3+}-doped $MAPbBr_3$, Bi^{3+}-doped $MAPbI_{2.5}Br_{0.5}$, and pristine (undoped) $MAPbI_3$ perovskite were step-by-step epitaxially grown on the surface of a $MAPbCl_3$ single-crystal substrate. All the Bi^{3+}-doped perovskite precursor solutions in this paper are uniformly added with a 10% mole concentration of Bi^{3+} salt because 10% Bi doping can cause a sufficient change in carrier properties without causing serious lattice distortion.[37,45] In fact, the real Bi^{3+} content in the grown perovskite crystal is lower than the nominal Bi^{3+} content (10%) in the feed solution, according to the X-ray photoelectron spectroscopy analysis results in Figure S1. The color of the as-grown epilayer after undergoing different steps of perovskite epitaxy changes from crimson to black, as seen in Figure 1b. The measured absorption spectra of each layer for the SCPH are shown in Figure 1c–f, and the estimated values of optical bandgaps (E_g) from the absorption edge using the Tauc-plot method are put inset. The arrangement of well-designed SCPH aims to construct a gradient bandgap structure with an energy funneling effect[46] that could filter different energy photons into the corresponding layer. Notably, the direction of epitaxy cannot be reversed (such as from I^- rich to Cl^- rich), which could be attributed to the huge differences in solubility behavior for hybrid halide perovskites in the solvents (DMSO, DMF, and GBL).[47]

A cross-sectional color change corresponding to the narrowing bandgaps of the fabricated $MAPbCl_3$/Bi-$MAPbBr_3$/Bi-$MAPbI_{2.5}Br_{0.5}$/$MAPbI_3$ SCPH is indicated by optical microscope photographs shown in Figure S2. By SEM, we more precisely observe that the as-fabricated $MAPbCl_3$/Bi-$MAPbBr_3$/Bi-$MAPbI_{2.5}Br_{0.5}$/$MAPbI_3$ SCPH with a total thickness of around 1.35 mm is a combination of four perovskite layers with different thickness, as shown in Figure 2a. The local enlarged SEM images at the interface of different materials prove a tight connection without any pin holes or gaps

https://doi.org/10.1021/acsphotonics.3c01768
ACS Photonics 2024, 11, 1252−1263

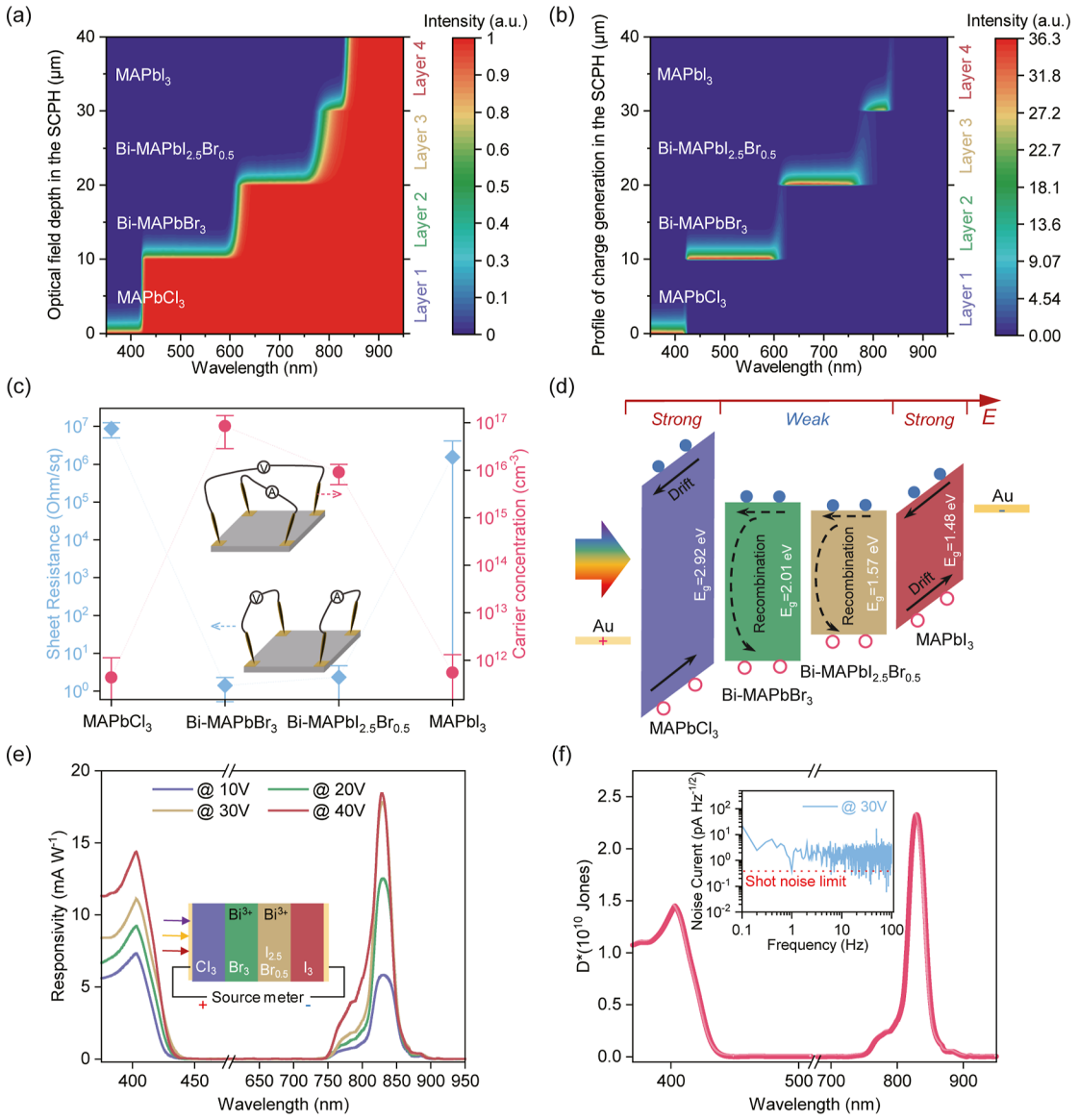

Figure 3. (a) Simulated two-dimensional cross-sectional optical field intensity distribution of the designed SCPH. Layers 1, 2, 3, and 4 represent the light passing through $MAPbCl_3$, Bi-$MAPbBr_3$, Bi-$MAPbI_{2.5}Br_{0.5}$, and $MAPbI_3$ perovskite single-crystalline films, respectively. (b) Simulated charge-carrier generation profile in the designed SCPH based on optical field distribution in (a). (c) Charge concentration (n) and sheet resistance (R) changes of the four perovskite layers in the SCPH. (d) Schematic diagrams illustrating the working principles of the dual-band SCPH PD operated at an external bias. (e) Response spectra of the fabricated SCPH based device under various external voltage bias. Inset: schematic of the response spectra measurement for the SCPH device. (f) Specific detectivity spectra (D^*) under an applied voltage of 30 V. Inset: noise current was extracted from the Fourier transform of dark current.

between two kinds of perovskite, which contributes to reducing the trap density and carrier recombination at the interface. Furthermore, EDX line scanning results of the halogen elements for the whole SCPH cross-section are displayed in Figure 2b, and the measured intensity ratio of Cl, Br, and I elements to all halogen reveals that four different perovskite layers of pure Cl, pure Br, mixed I with Br, and pure I were combined together successfully. Significantly, the halogen content will go through a gradient change until stable to expected halide content of perovskites epilayer, which is attributed to occurring inevitable halogen ions exchange during the LPE process.[43] The gradient halide region at each heterojunction interface all remains tens of micrometers thick without further obvious enlargement for the as-fabricated SCPH storing in room temperature after about 3 months, as proved in Figure S3. To investigate the crystallographic relationships between the four layers of the as-fabricated SCPH, XRD patterns of $MAPbCl_3$, Bi-$MAPbBr_3$, Bi-$MAPbI_{2.5}Br_{0.5}$, and $MAPbI_3$ are shown in Figure 2c in their freestanding form. For $MAPbCl_3$ and Bi-$MAPbBr_3$, it shows an apparent diffraction pattern from a cubic phase with a $Pm\bar{3}m$ space group, while Bi-$MAPbI_{2.5}Br_{0.5}$ and $MAPbI_3$ appear to be tetragonal phase with a $I4/m$ space group. A phase transition occurs at the interface between Bi-$MAPbBr_3$ and Bi-$MAPbI_{2.5}Br_{0.5}$ perovskite layers in the SCPH. Though analysis of diffraction peaks position, it indicates that the in-plane configuration of as-fabricated SCPH keeps an epitaxial relationship as $MAPbCl_3$ (100)||Bi-$MAPbBr_3$ (100)||Bi-$MAPbI_{2.5}Br_{0.5}$ (100)||$MAPbI_3$ (100). The tetragonal phase can be treated as a pseudocubic phase for the lattice parameter

https://doi.org/10.1021/acsphotonics.3c01768
ACS Photonics 2024, 11, 1252−1263

calculation, because tetragonal phase can transition from the cubic phase by slightly rotating the PbI_6 octahedra along the *c*-axis <001> on the (001) plane while maintaining their corner-sharing connectivity.[48,49] According to Bragg's law, we obtained the lattice constants of $MAPbCl_3$, Bi-$MAPbBr_3$, Bi-$MAPbI_{2.5}Br_{0.5}$ and $MAPbI_3$ as around 5.67, 5.89, 6.13, and 6.26 Å, respectively. In addition, the lattice mismatch factors (f) between the epilayer and substrate, calculated by the equation

$$f = \frac{a_e - a_s}{a_e}$$

where a_e and a_s are the lattice constants of epilayer and substrate, respectively. Lattice mismatch factors between adjacent perovskite layers are all estimated to be no more than 4%, as seen in Figure 2d, which confirms the feasibility of epitaxy in constructing the lattice-matched $MAPbCl_3$/Bi-$MAPbBr_3$/Bi-$MAPbI_{2.5}Br_{0.5}$/$MAPbI_3$ SCPH. However, $MAPbI_3$ films cannot immediately grow on the $MAPbCl_3$ crystal substrate by the LPE method due to a large lattice mismatch (~10%) between the two kinds of perovskites. The charge transport properties of each perovskite single crystal layer for the SCPH could be evaluated by PL spectra and TRPL decay measurements, as shown in Figure S4a,b, respectively. The PL intensity of Bi-doped $MAPbBr_3$ and Bi-doped $MAPbI_{2.5}Br_{0.5}$ layers reduce substantially contrast with pristine perovskite $MAPbCl_3$ and $MAPbI_3$ layers, indicating greatly increased nonradiative recombination centers in Bi-doped perovskite crystals. The faster PL decay for the Bi-doped perovskite layer indicates a shorter charge carrier lifetime due to increased defect states. All our findings are consistent with previous works.[45,50]

To further understand the absorption and charge carrier generation in the SCPH device, a simplified and ideal $MAPbCl_3$/Bi-$MAPbBr_3$/Bi-$MAPbI_{2.5}Br_{0.5}$/$MAPbI_3$ SCPH with a thickness of each perovskite layer as 10 μm was built for simulation. Suppose the optical field intensity distribution in the SCPH follows the Beer–Lambert law

$$I(x) = I_0\, e^{-\alpha x}$$

where I_0 is the incident light intensity through the incident face, $I(x)$ is the light intensity at coordinate position x, and α is the light absorption coefficient.[9] Based on the obtained absorption data of the four kinds perovskite layers, when light is incident from $MAPbCl_3$ side, the simulated normalized optical field intensity distributions (wavelength range from 350 to 950 nm) in the SCPH with four different bandgaps perovskite photosensitive layers are shown in Figure 3a. For UV light with wavelength of about 420 nm, it was almost absorbed in the first layer of $MAPbCl_3$ perovskite. For visible light penetrated through the first layer, a part of it was absorbed by the second layer of Bi-$MAPbBr_3$ perovskite, and the remaining part was absorbed by the third layer of Bi-$MAPbI_{2.5}Br_{0.5}$ perovskite. Only some near-infrared photons penetrated through the first three layers could be absorbed by the fourth layer of $MAPbI_3$, while the photons with wavelengths larger than 850 nm will penetrate whole SCPH without attenuation. Assuming the carrier generation efficiency is 100%, the ratio ($G(x)$) of the carrier generated at position x to the incident photon number can be derived as[9]

$$G(x) = -\frac{\frac{dI(x)}{dx}}{I_0} = \alpha\, e^{-\alpha x}$$

The photogenerated carrier distribution can be calculated in the active layer according to the optical field intensity distribution, as plotted in Figure 3b. It confirms that charge carriers excited by photons with wavelength less than 420 nm, from 420 to 600 nm, from 600 to 755 nm and from 755 to 830 nm were focused on the several micrometers' depth surface of $MAPbCl_3$, Bi-$MAPbBr_3$, Bi-$MAPbI_{2.5}Br_{0.5}$, and $MAPbI_3$ layer, respectively, due to a large absorption coefficient ($10^4 \sim 10^5$ cm^{-1}).[51] We measured the resistivity and Hall effect of each kind of the perovskite layer for the SCPH using the van der Pauw method, and the corresponding test model is shown in the inset of Figure 3c. The measured major carrier concentration of Bi^{3+}-doped $MAPbBr_3$ and Bi^{3+}-doped $MAPbI_{2.5}Br_{0.5}$ is approximately 5 orders of magnitude larger than pristine $MAPbCl_3$ and $MAPbI_3$, while the sheet resistance of Bi^{3+}-doped $MAPbBr_3$ and Bi^{3+}-doped $MAPbI_{2.5}Br_{0.5}$ is approximately 7 orders of magnitude smaller than pristine $MAPbCl_3$ and $MAPbI_3$. Additionally, carrier mobility of each perovskite single crystal layer was also obtained from the results of hall effect measurement as shown in Figure S5. The carrier mobility between pristine perovskite layers and 10% Bi^{3+}-doped perovskite layers have not much difference, which is consistent with earlier reports.[45] According to voltage division law of series circuit, it can deduce that the applied electric field on the $MAPbCl_3$/Bi-$MAPbBr_3$/Bi-$MAPbI_{2.5}Br_{0.5}$/$MAPbI_3$ SCPH is mainly distributed in pristine $MAPbCl_3$ and $MAPbI_3$ region, which also could be qualitatively estimated according to voltage drops across the cross-sectional of the SCPH shown in Figure S6. The schematic diagrams illustrating the visible elimination, UV and NIR dual-band light detection using the SCPH based device with semitransparent gold films serving as the electrode are depicted in Figure 3d. Only charge carriers excited in the pristine $MAPbCl_3$ layer and $MAPbI_3$ layer can be drifted and collected under a relatively strong electric field, while the charge carriers excited by visible photons will be recombined due to absence of electric field in Bi^{3+}-doped $MAPbBr_3$ and Bi^{3+}-doped $MAPbI_{2.5}Br_{0.5}$ regions. The measured response spectra as shown in Figure 3e confirms a well dual band detection ability in broad UV region and narrow NIR region and band elimination ability in visible region for as-fabricated SCPH-based PD. The responsivity (R) refers to the ratio of photocurrent to the incident light intensity, which can be calculated as

$$R = \frac{I_{ph}}{P_{light}} = \mathrm{EQE}\cdot\frac{e}{h\nu}$$

where I_{ph} is the photocurrent, P_{light} is the incident light intensity, e is the elementary charge, h is Planck's constant, and ν is the frequency of the incident light. The value of responsivity at UV and NIR region increases due to larger collection efficiency under applying larger electric field, while remains nearly zero in the visible region no matter how the applied bias for the SCPH device. Furthermore, the external quantum efficiency (EQE) spectra of the SCPH based PD at various external bias are shown in Figure S7. By using Fast Fourier transform of the time dominated dark current, we achieved the noise power density of the fabricated SCPH dual-band PD at a bias of 30 V (inset of Figure 3f). The frequency-independent white noise instead of $1/f$ noise dominates the noise behavior indicating relatively few traps in the epitaxy fabricated SCPH.[22,52] The shot noise limit (i_s) was estimated

https://doi.org/10.1021/acsphotonics.3c01768
ACS Photonics 2024, 11, 1252−1263

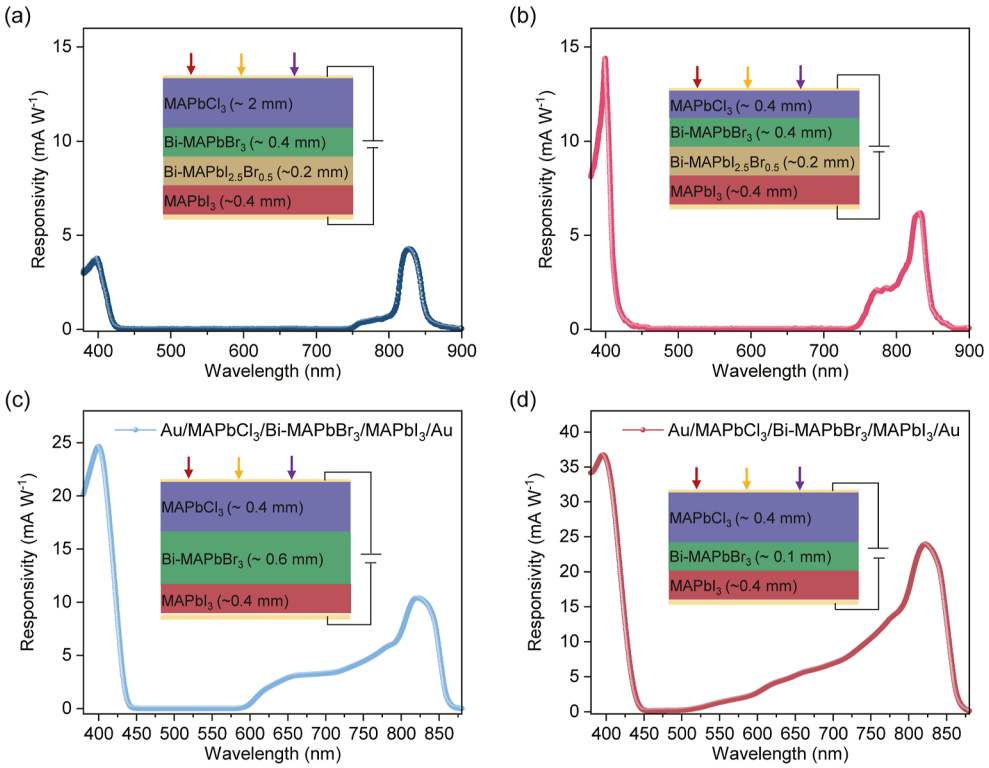

Figure 4. Response spectra of the $MAPbCl_3$/Bi-$MAPbBr_3$/Bi-$MAPbI_{2.5}Br_{0.5}$/$MAPbI_3$ SCPH device with a thick pristine perovskite layer (a) and thin pristine perovskite layer (b) at an external bias of 20 V. Response spectra of the $MAPbCl_3$/Bi-$MAPbBr_3$/$MAPbI_3$ three-layers SCPH device with a thick Bi^{3+} doped perovskite layer (c) and thin Bi^{3+} doped perovskite layer (d) at an external bias of 20 V. Inset: schematic of the response spectra measurement for the SCPH device with different structures and thickness.

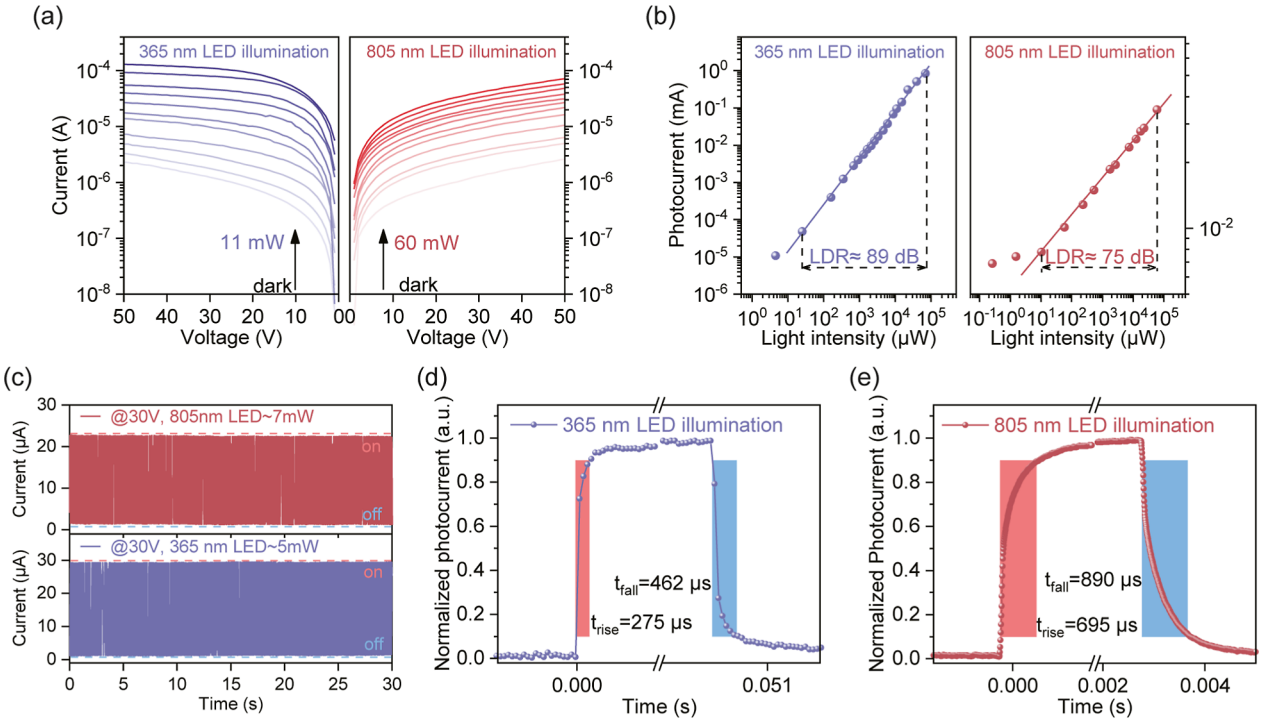

Figure 5. (a) Current−voltage (I−V) curves of the fabricated dual-band SCPH PD under 365 and 805 nm LED illuminating, respectively, with different power densities. (b) Photocurrent as a function of various light intensities for the fabricated dual-band SCPH PD at an applied bias of 30 V under 365 and 805 nm LED illumination, respectively. (c) Light on−off photoresponse curves of the fabricated dual-band SCPH PD under 365 and 805 nm LED illuminating, respectively. The transient photocurrent of the fabricated dual-band SCPH PD under 365 nm LED (d) and 805 nm LED (e) illuminating, respectively.

https://doi.org/10.1021/acsphotonics.3c01768
ACS Photonics 2024, 11, 1252−1263

of ~4.1 × 10^{-13} A $Hz^{-1/2}$ at a modulation frequency of 1 Hz by using the following equation

$$I_s = \sqrt{2eI_dB}$$

where I_d is the dark current and B is the bandwidth. Furthermore, the specific detectivity (D^*) can be calculated by

$$D^* = \frac{R\sqrt{AB}}{i_n}$$

based on the responsivity (R), effective area of the detector (A), and dark noise current (i_n). The D^* value is above 10^{10} jones (cm $Hz^{1/2}$ W^{-1}) in both UV and NIR bands, demonstrating the potential application of the device in weak light dual-color detection. Significantly, the dual band detection range does not show obvious changes when the thickness of pristine perovskite layers is different. By comparing the response spectra of devices with different pristine perovskite layer thicknesses in Figure 4a,b, we found the reduced thickness of the $MAPbCl_3$ layer from about 2 to 0.4 mm for the SCPH devices still keeps the same response range in the UV and NIR dual bands. Although the applied voltage bias is unchanged, the peak responsivity of the SCPH device in the UV and NIR ranges would rise with the reduced thickness of the $MAPbCl_3$ layer, which could be attributed to increased charge collection efficiency due to the larger electric field intensity on the thinner pristine perovskite layer. Moreover, a simpler three-layer SCPH device with a structure of $MAPbCl_3$/Bi-$MAPbBr_3$/$MAPbI_3$, as shown in Figure 4c, is also fabricated to compare the response spectra with the four-layer SCPH device with a structure of $MAPbCl_3$/Bi-$MAPbBr_3$/Bi-$MAPbI_{2.5}Br_{0.5}$/$MAPbI_3$. The three-layer SCPH device also reveals dual-band photodetection capability; however, its responsivity in the red light waveband rises markedly in comparison with the four-layer SCPH device due to the absence of the Bi-$MAPbI_{2.5}Br_{0.5}$ layer to block red light photons. It indicates that the Bi^{3+}-doped perovskite layers only absorb photons with energy above their bandgap but do not contribute photocurrent. We further fabricated a three-layer SCPH device by controlling the thickness of the Bi-$MAPbBr_3$ layer to only around 100 μm. The response spectrum presented in Figure 4d shows that the device with a thinner Bi-$MAPbBr_3$ layer has additional capacity to sense short-wavelength (around 550 nm) visible photons. The increased responsivity of short-wavelength visible photons could be due to the fact that some carriers generated in the thinner Bi-$MAPbBr_3$ layer diffuse to adjacent pristine perovskite layers and are collected under an electric field.

In addition, more photoelectric detection properties of the fabricated visible elimination, UV and NIR dual band SCPH based PD were estimated as following. Figure 5a shows the current−voltage (I−V) curves of the fabricated dual band SCPH device under UV monochromatic LED (~365 nm) illumination with the power density changing from 0 to 11 mW and NIR monochromatic LED (~805 nm) illumination with the power density changing from 0 to 60 mW. A relatively low dark current density and a high on/off ratio large than 100 under external bias are attributed to few traps in the lattice-matched single-crystalline heterojunction. Furthermore, the carrier mobility-lifetime product of the $MAPbCl_3$/Bi-$MAPbBr_3$/Bi-$MAPbI_{2.5}Br_{0.5}$/$MAPbI_3$ SCPH is evaluated as ~10^{-4} cm^2 V^{-1}, as shown in Figure S8 through the voltage dependence of the photocurrent fitted using a simplified Hecht equation[9]

$$I = I_0\mu\tau\frac{U}{d^2}(1 - e^{-d^2/\mu\tau U})$$

where I_0 is the saturated photocurrent, U is the applied voltage, d is the device thickness, and $\mu\tau$ is the mobility-lifetime product. The variation of photocurrent with the incident power measured by 365 and 805 nm LEDs for the fabricated dual band SCPH device is plotted in Figure 5b. The linear dynamic range (LDR) is commonly expressed on a logarithmic scale using the following equation

$$LDR = 20\log\frac{P_{high}}{P_{low}}$$

where P_{high} and P_{low} represent the highest and lowest light intensity within the fitted solid line, respectively. The values of LDR are measured as about 89 dB for 365 nm light illumination and 75 dB for 365 nm light illumination at an applied bias of 30 V. It is worth noting that the measured LDR might be under-valued due to the limited output power of the commercial LED. Figure 5c shows on−off curves of the fabricated dual-band SCPH PD under modulated 10 Hz square wave light illumination by 365 and 805 nm LED. The dark current and light current remain almost unchanged, indicating good response repeatability. Additionally, we also investigate the response's long-term stability after about 20 days with the SCPH device stored in ambient air conditions without any encapsulation, as shown in Figure S9. After the SCPH device was stored for a long time, its detection performance for UV light merely had a slight degeneration, but for NIR light, it degraded significantly, which could be due to the migration of mobile ions in $MAPbI_3$ and low tolerance to environmental factors such as moisture, oxygen, and illumination for $MAPbI_3$.[53] The transient photoresponses of the fabricated dual-band SCPH PD under 365 nm LED and 805 nm LED illuminating are shown in Figure 5d,e, respectively. Its response speed is evaluated by rise time and fall time, defined as the time for photocurrent to change from 10 to 90% of its maximum and vice versa. The rise time and fall time are measured in hundreds of micrometers and have the potential to be faster by increasing applied bias or further reducing the thickness of pristine layers in the SCPH, as shown in Figure S10.

As a promising and widely concerned communication technology, optical communication still suffers from severe data leakage due to inevitably scattering and refracting in all directions during open transmission.[18,20] For instance, if only through a single visible light band to convey information in open channels, the data signals will be easily filched just using a common low-band gap silicon-based PDs sensitive to visible photons as a receiver. Inspired by some previous works about encrypted optical communication technology,[19,29,33,36] we built a UV and NIR dual channel double encrypted optical communication code system based on the fabricated specific dual-band SCPH PD as receiver terminal, while three commercial monochromatic LEDs with different central wavelengths of 365 nm (UV), 520 nm (visible), and 805 nm (NIR) as the cyphertext signal emitter, noise signal emitter, and key signal emitter, respectively. In our double encrypted optical communication, cyphertext signals carried by UV light and noise signals carried by visible light are superposed

https://doi.org/10.1021/acsphotonics.3c01768
ACS Photonics 2024, 11, 1252−1263

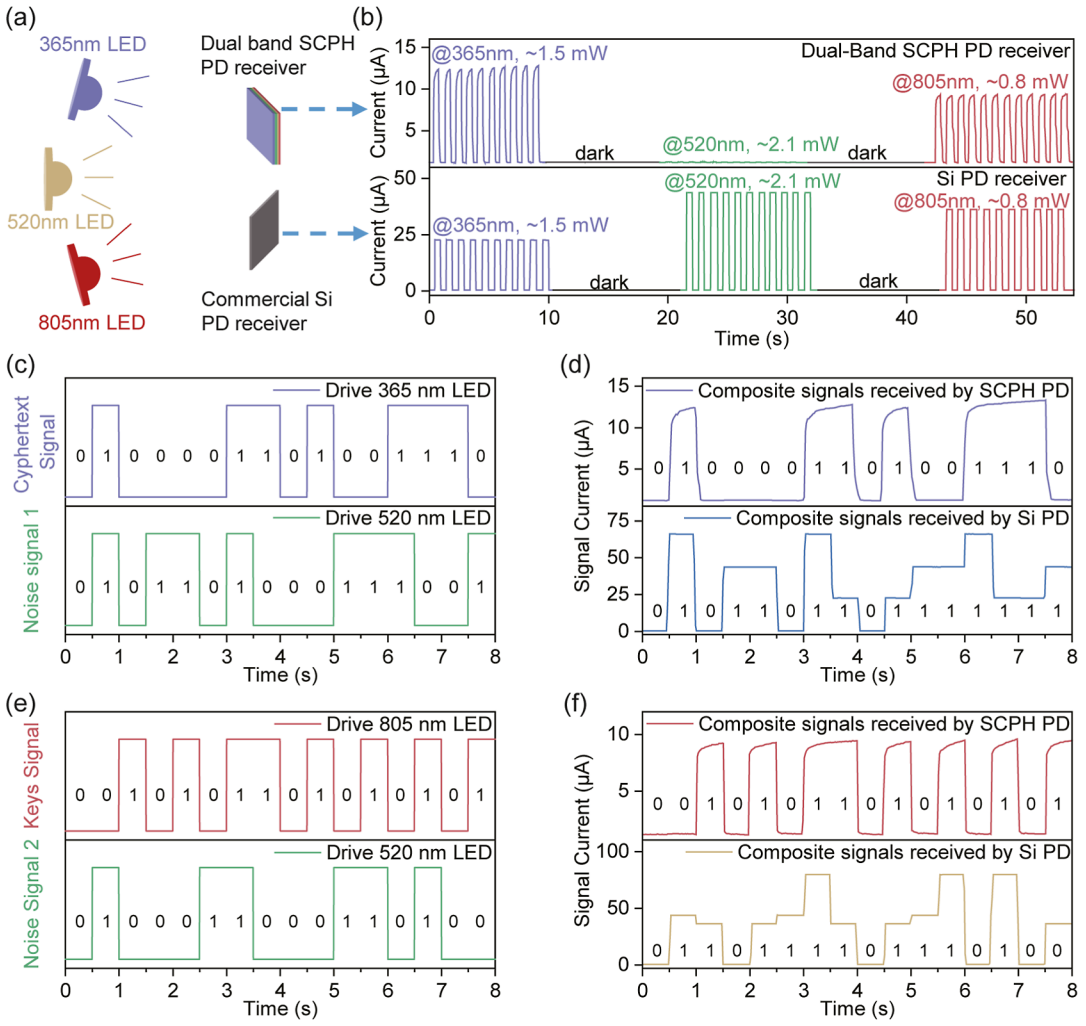

Figure 6. (a) Protype of the chaos light-based optical communication system for the fabricated dual-band SCPH PD and commercial Si PD. (b) Photocurrent intensity received by the fabricated dual-band SCPH PD and commercial Si PD, respectively, for 365, 520, and 805 nm monochromatic LED emitted light on−off signals. (c) Mixed light for encrypted cyphertext signal transmitting with corresponding code for driving 365 and 520 nm LED, respectively. (d) Contrast of photoresponse characteristics received by the dual-band SCPH PD and Si PD for mixed 365 and 520 nm light signal in (c). (e) Mixed light for encrypted key signal transmitting with corresponding code for driving 365 and 520 nm LED, respectively. (f) Contrast of photoresponse characteristics received by the dual-band SCPH PD and Si PD for mixed 805 and 520 nm light signal in (c).

together for the first encryption transmission, and then key signals carried by NIR light and noise signals carried by visible light are superposed together for the second encryption transmission. The double encrypted transmission process increases the difficulties of signal decoding; it is workable using a specific visible-elimination UV/NIR dual-band PD as the receiver terminal, while the eavesdropper hardly decodes valid signals by using common PDs as receivers under the condition of unknown correct modulation wavelengths. As shown in Figure 6a, to confirm the effectiveness of confidential signal transmission, a common commercial silicon (Si) photodiode is added beside our SCPH PD as a signal receiver. As shown in Figure 6b, when the three monochromatic LEDs are turned on and off step by step, the fabricated SCPH PD only receives the light signal emitted by the 365 nm LED and the 805 nm LED, while a commercial silicon PD responds to all three monochromatic LEDs due to the broad spectra photosensitivity shown in Figure S11. Theoretically, the as-fabricated specific dual-band SCPH PDs can receive the valid information carried by 365 nm UV light and 805 nm NIR light without 520 nm visible light interference, while the common commercial Si PDs will receive chaotic data that is useless. Furthermore, we verified the proposed double-encrypted optical communication with all the data processing procedures based on the binary system. For the received current signals by PDs, the dark current level signal and photocurrent level signal are defined as "0" and "1", respectively. First, in the encrypted cyphertext signal transmitting process, driver signals for 365 and 520 nm LEDs are presented in Figure 6c to output mixed light signals including cyphertext signals (ASCII codes means "CN") and random noise signals. Our fabricated specific dual-band PD received correct current signals as same as cyphertext signals emitted by 365 nm LEDs, while the commercial Si PD received coherent current signals from 365 and 520 nm lights that cannot be correctly decoded using ASCII codes, as seen in Figure 6d. Then similarly, in the encrypted key signal transmitting process, mixed light signals, including key signals, and random noise signals are output for transmitting encrypted key signals, and the driving signals for 805 and 520 nm LEDs are presented in Figure 6e. The correct key signals can be

https://doi.org/10.1021/acsphotonics.3c01768
ACS Photonics 2024, 11, 1252−1263

recorded and successfully decoded as "+U" using ASCII codes by our specific dual-band SCPH PD, while the correct key signals cannot be received by the commercial Si PD due to the interference of 520 nm light, as shown in Figure 6f. Only correct cyphertext data and correct key data are received together; the final valid original plaintext can be further decoded according to the preagreed algorithm between cyphertext and key. Predictably, using NPDs with a single waveband response as receivers also hardly obtains a valid original plaintext in double-encrypted optical communication if the correct modulation wavelength is not known, as shown in Figure S12. It is clear that visible elimination, UV, and NIR dual-band SCPH PD can decode encrypted information accurately from chaotic light signals based on its own specific photodetection characteristics and contribute to achieving secure optical communication without relying on complicated algorithms.

CONCLUSIONS

In summary, in this work, we report a novel dual-band PD based on $MAPbCl_3$/Bi-$MAPbBr_3$/Bi-$MAPbI_{2.5}Br_{0.5}$/$MAPbI_3$ SCPH, which senses to both a broad range (cutoff wavelengths of 425 nm) corresponding to UV lights and a narrow range (wavelengths from 750 to 880 nm) corresponding to NIR lights, while blinding to visible light in-between the two wavebands. The special ability of visible elimination, UV/NIR dual band detection, is attributed to forming a discontinuous electric field distributed in the SCPH by controlling the doping position of bismuth. The lattice-matched dual-band SCPH could be fabricated facially by a low-cost LPE process without any complex technology and shows considerable photodetection performance, such as R of tens of mA W^{-1}, LDR of around 80 dB, D^* greater than 10^{10} Jones, and response speed of hundreds of microseconds. Benefiting from the high photosensitivity in the UV and NIR wavelength regions and the rejected response in the visible wavelength regions for the dual-band SCPH PD, we built a double encryption system for security optical communication by hiding the cyphertext signals and key signals in the chaos signals of the transmitter light. For encrypted light signal transmitting, mixed UV/visible light, including encrypted cyphertext signals, and mixed NIR/visible light, including key signals, are sent separately. The as-fabricated specific visible-elimination UV/NIR dual-band SCPH PD presents the accurate and confidential identification ability of signal decoding from chaos lights and realizes secure optical communication that is more superior than common single broad and narrow band PDs.

ASSOCIATED CONTENT

Supporting Information

The Supporting Information is available free of charge at https://pubs.acs.org/doi/10.1021/acsphotonics.3c01768.

Materials and methods; details of all experimental procedures; XPS analysis; cross-sectional optical microscope photographs; EDX line mapping of heterojunction interfaces; PL spectroscopy spectra; mobility measured by hall effect; potential drop measurement and EQE spectra of as-fabricated PSCH; Hecht-equation fitting; long-term device stability; voltage and thickness dependent transient photocurrent; typical response spectra of Si photodiodes; and logic results diagram of the double-encrypted optical communication (PDF)

AUTHOR INFORMATION

Corresponding Authors

Xin Wang − *School of Electronic Science and Engineering, Joint International Research Laboratory of Information Display and Visualization, Southeast University, Nanjing 210096, China;* orcid.org/0000-0003-2496-2872; Email: xinw@seu.edu.cn

Wei Lei − *School of Electronic Science and Engineering, Joint International Research Laboratory of Information Display and Visualization, Southeast University, Nanjing 210096, China*; Email: lw@seu.edu.cn

Authors

Yuzhu Pan − *School of Electronic Science and Engineering, Joint International Research Laboratory of Information Display and Visualization, Southeast University, Nanjing 210096, China;* orcid.org/0000-0002-0685-2840

Dan Zhang − *School of Electronic Science and Engineering, Joint International Research Laboratory of Information Display and Visualization, Southeast University, Nanjing 210096, China*

Ziyu Wei − *School of Electronic Science and Engineering, Joint International Research Laboratory of Information Display and Visualization, Southeast University, Nanjing 210096, China*

Yubing Xu − *School of Electronic Science and Engineering, Joint International Research Laboratory of Information Display and Visualization, Southeast University, Nanjing 210096, China*

Yuwei Li − *School of Electronic Science and Engineering, Joint International Research Laboratory of Information Display and Visualization, Southeast University, Nanjing 210096, China*

Qing Li − *School of Electronic Science and Engineering, Joint International Research Laboratory of Information Display and Visualization, Southeast University, Nanjing 210096, China*

Zhiwei Zhao − *School of Electronic Science and Engineering, Joint International Research Laboratory of Information Display and Visualization, Southeast University, Nanjing 210096, China*

Zhuoya Zhu − *School of Electronic Science and Engineering, Joint International Research Laboratory of Information Display and Visualization, Southeast University, Nanjing 210096, China*

Byung Seong Bae − *Department of Electronics & Display Engineering Hoseo University, Asan City, Chungnam 31499, Republic of Korea;* orcid.org/0000-0002-3328-0286

Damian Chinedu Onwudiwe − *Department of Chemistry, School of Mathematics and Physical Sciences, Faculty of Natural and Agricultural Sciences North-West University Mafikeng Campus, Mmabatho 2735, South Africa*

Xiaobao Xu − *School of Electronic Science and Engineering, Joint International Research Laboratory of Information Display and Visualization, Southeast University, Nanjing 210096, China;* orcid.org/0000-0001-5378-5604

Complete contact information is available at: https://pubs.acs.org/10.1021/acsphotonics.3c01768

Author Contributions

This work was conceptualized by Yuzhu Pan and Xin Wang. Yuzhu Pan, Dan Zhang, and ZiYu Wei contributed to the fabrication of the devices. Yuzhu Pan conducted the character-

https://doi.org/10.1021/acsphotonics.3c01768
ACS Photonics 2024, 11, 1252−1263

ization of the optical and electrical properties. Yubing Xu and Yuwei Li helped with the testing of the practical application of photodetectors. Yuzhu Pan and Xin Wang analyzed the results. Yuzhu Pan wrote this manuscript. All authors commented on the manuscript.

Notes

The authors declare no competing financial interest.

■ ACKNOWLEDGMENTS

This work is financially supported by the International cooperative research project of Jiangsu province (BZ2022008), the National Key Research and Development Program of China (2022YFE0139100), the National Natural Science Foundation Project of China (62175028, 51879042, 61674029, 12005038, and 12375306), the China Postdoctoral Foundation funded project (2023T160106 and 2023M730555), and the Postgraduate Research & Practice Innovation Program of Jiangsu Province (KYCK22_0229).

■ REFERENCES

(1) Li, Z.; Yan, T.; Fang, X. Low-Dimensional Wide-Bandgap Semiconductors for UV Photodetectors. *Nat. Rev. Mater.* **2023**, *8* (9), 587−603.

(2) Ren, H.; Chen, J. D.; Li, Y. Q.; Tang, J. X. Recent Progress in Organic Photodetectors and their Applications. *Adv. Sci.* **2021**, *8* (1), 2002418.

(3) Chen, Y.; Su, L.; Jiang, M.; Fang, X. Switch Type PANI/ZnO Core-Shell Microwire Heterojunction for UV Photodetection. *J. Mater. Sci. Technol.* **2022**, *105*, 259−265.

(4) Li, Z.; Trendafilov, S.; Zhang, F.; Allen, M. S.; Allen, J. W.; Dev, S. U.; Pan, W.; Yu, Y.; Gao, Q.; Yuan, X.; et al. Broadband GaAsSb Nanowire Array Photodetectors for Filter-Free Multispectral Imaging. *Nano Lett.* **2021**, *21* (17), 7388−7395.

(5) Dandin, M.; Abshire, P.; Smela, E. Optical Filtering Technologies for Integrated Fluorescence Sensors. *Lab Chip* **2007**, *7* (8), 955−977.

(6) Siegmund, B.; Mischok, A.; Benduhn, J.; Zeika, O.; Ullbrich, S.; Nehm, F.; Böhm, M.; Spoltore, D.; Fröb, H.; Körner, C.; et al. Organic Narrowband Near-Infrared Photodetectors Based on Intermolecular Charge-Transfer Absorption. *Nat. Commun.* **2017**, *8* (1), 15421.

(7) Tsai, W.-L.; Chen, C.-Y.; Wen, Y.-T.; Yang, L.; Cheng, Y.-L.; Lin, H.-W. Band Tunable Microcavity Perovskite Artificial Human Photoreceptors. *Adv. Mater.* **2019**, *31* (24), 1900231.

(8) Xing, S.; Nikolis, V. C.; Kublitski, J.; Guo, E.; Jia, X.; Wang, Y.; Spoltore, D.; Vandewal, K.; Kleemann, H.; Benduhn, J.; et al. Miniaturized VIS-NIR Spectrometers Based on Narrowband and Tunable Transmission Cavity Organic Photodetectors with Ultrahigh Specific Detectivity above 10(14) Jones. *Adv. Mater.* **2021**, *33* (44), No. e2102967.

(9) Fang, Y.; Dong, Q.; Shao, Y.; Yuan, Y.; Huang, J. Highly Narrowband Perovskite Single-Crystal Photodetectors Enabled by Surface-Charge Recombination. *Nat. Photonics* **2015**, *9* (10), 679−686.

(10) Armin, A.; Jansen-van Vuuren, R. D.; Kopidakis, N.; Burn, P. L.; Meredith, P. Narrowband Light Detection via Internal Quantum Efficiency Manipulation of Organic Photodiodes. *Nat. Commun.* **2015**, *6* (1), 6343.

(11) Zhao, Z.; Xu, C.; Ma, Y.; Ma, X.; Zhu, X.; Niu, L.; Shen, L.; Zhou, Z.; Zhang, F. Filter-Free Narrowband Photomultiplication-Type Planar Heterojunction Organic Photodetectors. *Adv. Funct. Mater.* **2023**, *33* (9), 2212149.

(12) Wang, W.; Zhang, F.; Du, M.; Li, L.; Zhang, M.; Wang, K.; Wang, Y.; Hu, B.; Fang, Y.; Huang, J. Highly Narrowband Photomultiplication Type Organic Photodetectors. *Nano Lett.* **2017**, *17* (3), 1995−2002.

(13) Xie, B.; Xie, R.; Zhang, K.; Yin, Q.; Hu, Z.; Yu, G.; Huang, F.; Cao, Y. Self-Filtering Narrowband High Performance Organic Photodetectors Enabled by Manipulating Localized Frenkel Exciton Dissociation. *Nat. Commun.* **2020**, *11* (1), 2871.

(14) Sun, B.; Zhou, G.; Wang, Y.; Xu, X.; Tao, L.; Zhao, N.; Tsang, H. K.; Wang, X.; Chen, Z.; Xu, J. B. Ultra-Narrowband Photodetector with High Responsivity Enabled by Integrating Monolayer J-Aggregate Organic Crystal with Graphene. *Adv. Opt. Mater.* **2021**, *9* (17), 210015.

(15) Pan, Y.; Wang, X.; Liao, Y.; Xu, Y.; Li, Y.; Li, Q.; Zhang, X.; Chen, J.; Zhu, Z.; Zhao, Z.; et al. Epitaxial Perovskite Single-Crystalline Heterojunctions for Filter-Free Ultra-Narrowband Detection with Tunable Spectral Responses. *ACS Appl. Mater. Interfaces* **2022**, *14* (44), 50331−50342.

(16) Cao, F.; Yan, T.; Li, Z.; Wu, L.; Fang, X. Dual-Band Perovskite Bulk Heterojunction Self-Powered Photodetector for Encrypted Communication and Imaging. *Adv. Opt. Mater.* **2022**, *10* (18), 2200786.

(17) Dai, M.; Chen, H.; Feng, R.; Feng, W.; Hu, Y.; Yang, H.; Liu, G.; Chen, X.; Zhang, J.; Xu, C.-Y.; et al. A Dual-Band Multilayer InSe Self-Powered Photodetector with High Performance Induced by Surface Plasmon Resonance and Asymmetric Schottky Junction. *ACS Nano* **2018**, *12* (8), 8739−8747.

(18) Liu, S.; Jiao, S.; Zhao, Y.; Lu, H.; Yang, S.; Wang, D.; Gao, S.; Wang, J.; Zhao, L. Bi_2O_3 Layer-Integrated, Double-Sided Responsive, Waveband-Discriminated Perovskite Photodetector for Encrypted Optical Communication. *Adv. Opt. Mater.* **2023**, *11* (21), 2300831.

(19) Yan, T.; Li, Z.; Su, L.; Wu, L.; Fang, X. Bidirectional and Dual-Mode Organic Photodetector Enables Secure Ultraviolet Communication. *Adv. Funct. Mater.* **2023**, *33* (31), 2302746.

(20) Huang, B.; Liu, J.; Han, Z.; Gu, Y.; Yu, D.; Xu, X.; Zou, Y. High-Performance Perovskite Dual-Band Photodetectors for Potential Applications in Visible Light Communication. *ACS Appl. Mater. Interfaces* **2020**, *12* (43), 48765−48772.

(21) Xu, X.; Deng, W.; Zhang, X.; Huang, L.; Wang, W.; Jia, R.; Wu, D.; Zhang, X.; Jie, J.; Lee, S. T. Dual-Band, High-Performance Phototransistors from Hybrid Perovskite and Organic Crystal Array for Secure Communication Applications. *ACS Nano* **2019**, *13* (5), 5910−5919.

(22) Li, L.; Chen, H.; Fang, Z.; Meng, X.; Zuo, C.; Lv, M.; Tian, Y.; Fang, Y.; Xiao, Z.; Shan, C.; et al. An Electrically Modulated Single-Color/Dual-Color Imaging Photodetector. *Adv. Mater.* **2020**, *32* (24), No. e1907257.

(23) Tang, X.; Ackerman, M. M.; Chen, M.; Guyot-Sionnest, P. Dual-Band Infrared Imaging Using Stacked Colloidal Quantum Dot Photodiodes. *Nat. Photonics* **2019**, *13* (4), 277−282.

(24) Su, L.; Chen, H.; Xu, X.; Fang, X. Novel BeZnO Based Self-Powered Dual-Color UV Photodetector Realized via a One-Step Fabrication Method. *Laser Photonics Rev.* **2017**, *11* (6), 1700222.

(25) Chiang, J. C.; Li, S. S.; Singh, A. A Two-Stack Indirect-Barrier/Triple-Coupled Quantum Well Infrared Detector for Mid-Wavelength and Long-Wavelength Infrared Dual Band Detection. *Appl. Phys. Lett.* **1997**, *71* (24), 3546−3548.

(26) Lan, Z.; Lei, Y.; Chan, W. K. E.; Chen, S.; Luo, D.; Zhu, F. Near-Infrared and Visible Light Dual-Mode Organic Photodetectors. *Sci. Adv.* **2020**, *6* (5), No. eaaw8065.

(27) Wang, P.; Liu, S.; Luo, W.; Fang, H.; Gong, F.; Guo, N.; Chen, Z. G.; Zou, J.; Huang, Y.; Zhou, X.; et al. Arrayed Van Der Waals Broadband Detectors for Dual-Band Detection. *Adv. Mater.* **2017**, *29* (16), 1604439.

(28) Haddadi, A.; Dehzangi, A.; Chevallier, R.; Adhikary, S.; Razeghi, M. Bias-Selectable nBn Dual-Band Long-/Very Long-Wavelength Infrared Photodetectors based on $InAs/InAs_{1-x}Sb_x/AlAs_{1-x}Sb_x$ Type-II Superlattices. *Sci. Rep.* **2017**, *7* (1), 3379.

(29) Cao, F.; Li, Z.; Liu, X.; Shi, Z.; Fang, X. Air Induced Formation of $Cs_3Bi_2Br_9/Cs_3BiBr_6$ Bulk Heterojunction and Its Dual-band Photodetection Abilities for Light Communication. *Adv. Funct. Mater.* **2022**, *32* (46), 2206151.

https://doi.org/10.1021/acsphotonics.3c01768
ACS Photonics 2024, 11, 1252−1263

(30) Wang, H.; Kim, D. H. Perovskite-Based Photodetectors: Materials and Devices. *Chem. Soc. Rev.* **2017**, *46* (17), 5204−5236.
(31) Wang, F.; Zou, X.; Xu, M.; Wang, H.; Wang, H.; Guo, H.; Guo, J.; Wang, P.; Peng, M.; Wang, Z.; et al. Recent Progress on Electrical and Optical Manipulations of Perovskite Photodetectors. *Adv. Sci.* **2021**, *8* (14), No. e2100569.
(32) Wu, W.; Lu, H.; Han, X.; Wang, C.; Xu, Z.; Han, S. T.; Pan, C. Recent Progress on Wavelength-Selective Perovskite Photodetectors for Image Sensing. *Small Methods* **2023**, *7* (4), 2201499.
(33) Cheng, W.; Tian, W.; Cao, F.; Li, L. Self-Powered Bifunctional Perovskite Photodetectors with Both Broadband and Narrowband Photoresponse. *InfoMat* **2022**, *4* (11), No. e12348.
(34) Zhao, J.; Wang, X.; Xu, Y.; Pan, Y.; Li, Y.; Chen, J.; Li, Q.; Zhang, X.; Zhu, Z.; Zhao, Z.; et al. Electrically Modulated Near-Infrared/Visible Light Dual-Mode Perovskite Photodetectors. *ACS Appl. Mater. Interfaces* **2022**, *14* (22), 25824−25833.
(35) He, J.; Liu, Y.; Li, Z.; Ji, Z.; Yan, G.; Zhao, C.; Mai, W. Achieving Dual-Color Imaging by Dual-Band Perovskite Photodetectors Coupled with Algorithms. *J. Colloid Interface Sci.* **2022**, *625*, 297−304.
(36) Wu, Y.; Li, X.; Wei, Y.; Gu, Y.; Zeng, H. Perovskite Photodetectors with Both Visible-Infrared Dual-Mode Response and Super-Narrowband Characteristics Towards Photo-Communication Encryption Application. *Nanoscale* **2018**, *10* (1), 359−365.
(37) Abdelhady, A. L.; Saidaminov, M. I.; Murali, B.; Adinolfi, V.; Voznyy, O.; Katsiev, K.; Alarousu, E.; Comin, R.; Dursun, I.; Sinatra, L.; et al. Heterovalent Dopant Incorporation for Bandgap and Type Engineering of Perovskite Crystals. *J. Phys. Chem. Lett.* **2016**, *7* (2), 295−301.
(38) Kundu, S.; Zhang, D.; Askar, A. M.; Moloney, E. G.; Adachi, M. M.; Nadeem, A.; Moradi, S.; Yeddu, V.; Abdelhady, A. L.; Voznyy, O.; et al. Bismuth Stabilizes the α-Phase of Formamidinium Lead Iodide Perovskite Single Crystals. *ACS Mater. Lett.* **2022**, *4* (4), 707−712.
(39) Zhou, Y.; Yong, Z. J.; Zhang, K. C.; Liu, B. M.; Wang, Z. W.; Hou, J. S.; Fang, Y. Z.; Zhou, Y.; Sun, H. T.; Song, B. Ultrabroad Photoluminescence and Electroluminescence at New Wavelengths from Doped Organometal Halide Perovskites. *J. Phys. Chem. Lett.* **2016**, *7* (14), 2735−2741.
(40) Haque, M. A.; Li, J. L.; Abdelhady, A. L.; Saidaminov, M. I.; Baran, D.; Bakr, O. M.; Wei, S. H.; Wu, T. Transition from Positive to Negative Photoconductance in Doped Hybrid Perovskite Semiconductors. *Adv. Opt. Mater.* **2019**, *7* (22), 1900865.
(41) Wang, X.; Li, Y.; Xu, Y.; Pan, Y.; Zhu, C.; Zhu, D.; Wu, Y.; Li, G.; Zhang, Q.; Li, Q.; et al. Solution-Processed Halide Perovskite Single Crystals with Intrinsic Compositional Gradients for X-ray Detection. *Chem. Mater.* **2020**, *32* (12), 4973−4983.
(42) Wang, X.; Xu, Y.; Pan, Y.; Li, Y.; Xu, J.; Chen, J.; Wu, J.; Li, Q.; Zhang, X.; Zhao, Z.; et al. Low-Noise X-ray PIN Photodiodes Made of Perovskite Single Crystals by Solution-Processed Dopant Incorporated Epitaxial Growth. *Nano Energy* **2021**, *89*, 106311.
(43) Pan, Y.; Wang, X.; Xu, Y.; Chai, S.; Wu, J.; Zhao, Z.; Li, Q.; Wu, J.; Chen, J.; Zhu, Z.; et al. Epitaxy Growth of $MAPbBr_xCl_{3-x}$ Single-Crystalline Perovskite Films Toward Spectral Selective Detection in Both Broadband and Narrowband Ranges. *J. Mater. Chem. C* **2023**, *11* (40), 13763−13773.
(44) Sciamanna, M.; Shore, K. A. Physics and Applications of Laser Diode Chaos. *Nat. Photonics* **2015**, *9* (3), 151−162.
(45) Meng, R.; Wu, G.; Zhou, J.; Zhou, H.; Fang, H.; Loi, M. A.; Zhang, Y. Understanding the Impact of Bismuth Heterovalent Doping on the Structural and Photophysical Properties of $CH_3NH_3PbBr_3$ Halide Perovskite Crystals with Near-IR Photoluminescence. *Chem.—Eur. J.* **2019**, *25* (21), 5480−5488.
(46) Ou, Q.; Bao, X.; Zhang, Y.; Shao, H.; Xing, G.; Li, X.; Shao, L.; Bao, Q. Band Structure Engineering in Metal Halide Perovskite Nanostructures for Optoelectronic Applications. *Nano Mater. Sci.* **2019**, *1* (4), 268−287.
(47) Petrov, A. A.; Ordinartsev, A. A.; Fateev, S. A.; Goodilin, E. A.; Tarasov, A. B. Solubility of Hybrid Halide Perovskites in DMF and DMSO. *Molecules* **2021**, *26* (24), 7541.
(48) Zhang, Y.; Liu, Y.; Li, Y.; Yang, Z.; Liu, S. Perovskite $CH_3NH_3Pb(Br_xI_{1-x})_3$ Single Crystals with Controlled Composition for Fine-Tuned Bandgap Towards Optimized Optoelectronic Applications. *J. Mater. Chem. C* **2016**, *4* (39), 9172−9178.
(49) Ji, L.; Hsu, H.-Y.; Lee, J. C.; Bard, A. J.; Yu, E. T. High-Performance Photodetectors Based on Solution-Processed Epitaxial Grown Hybrid Halide Perovskites. *Nano Lett.* **2018**, *18* (2), 994−1000.
(50) Nayak, P. K.; Sendner, M.; Wenger, B.; Wang, Z.; Sharma, K.; Ramadan, A. J.; Lovrincic, R.; Pucci, A.; Madhu, P. K.; Snaith, H. J. Impact of Bi(3+) Heterovalent Doping in Organic-Inorganic Metal Halide Perovskite Crystals. *J. Am. Chem. Soc.* **2018**, *140* (2), 574−577.
(51) Laamari, M. E.; Cheknane, A.; Benghia, A.; Hilal, H. S. Optimized Opto-Electronic and Mechanical Properties of Orthorhombic Methylamunium Lead Halides ($MAPbX_3$) (X = I, Br and Cl) for Photovoltaic Applications. *Sol. Energy* **2019**, *182*, 9−15.
(52) Fang, Y.; Huang, J. Resolving Weak Light of Sub-picowatt per Square Centimeter by Hybrid Perovskite Photodetectors Enabled by Noise Reduction. *Adv. Mater.* **2015**, *27* (17), 2804−2810.
(53) McGovern, L.; Futscher, M. H.; Muscarella, L. A.; Ehrler, B. Understanding the Stability of $MAPbBr_3$ versus $MAPbI_3$: Suppression of Methylammonium Migration and Reduction of Halide Migration. *J. Phys. Chem. Lett.* **2020**, *11* (17), 7127−7132.

https://doi.org/10.1021/acsphotonics.3c01768
ACS Photonics 2024, 11, 1252−1263